8-12-2022

Stability Characteristics of the Mesopause Region Above the Andes

Fan Yang
Embry-Riddle Aeronautical University, yangf1@erau.edu

Alan Z. Liu
Embry Riddle Aeronautical University, liuz2@erau.edu

Scholarly Commons Citation

Yang, F., & Liu, A. Z. (2022). Stability characteristics of the mesopause region above the Andes. Journal of Geophysical Research: Space Physics, 127, e2022JA030315. https://doi. org/10.1029/2022JA030315

JGR Space Physics

RESEARCH ARTICLE
10.1029/2022JA030315

Stability Characteristics of the Mesopause Region Above the Andes

Fan Yang[1] **and Alan Z. Liu**[1]

[1]Department of Physical Sciences, Center for Space and Atmospheric Research, Embry-Riddle Aeronautical University, Daytona Beach, FL, USA

Key Points:

- Contributions from buoyancy frequency and wind shear to Richardson number are presented
- Biases of the instability probabilities due to photon noise have been analyzed
- Gravity waves with different frequency effects the generation of dynamical and convective instabilities

Correspondence to:

A. Z. Liu,
alan.liu@erau.edu

Citation:

Yang, F., & Liu, A. Z. (2022). Stability characteristics of the mesopause region above the Andes. *Journal of Geophysical Research: Space Physics*, *127*, e2022JA030315. https://doi.org/10.1029/2022JA030315

Received 24 JAN 2022
Accepted 12 AUG 2022

Abstract We report a detailed analysis of atmospheric stabilities in the mesopause region (85–100 km) based on over 2,000 hr of high-resolution temperature and horizontal wind measurements made with a Na lidar at the Andes Lidar Observatory, located in Cerro Pachón, Chile (30.25°S, 70.74°W). The square of Brunt–Väisälä frequency and the Richardson number are calculated, and occurrence probabilities of convective and dynamic instabilities are derived. An approach to assess the biases due to measurement uncertainties is used to obtain more accurate occurrence probabilities. The overall occurrence probabilities of convective and dynamic instabilities are 2.7% and 6.7%, respectively. High-, medium-, and low- frequency gravity wave (GW) contributions to these probabilities are isolated, which show that the high-frequency GWs contribute most but simultaneous presence of high- and medium frequency GWs is much more effective in increasing the probabilities. Convective and dynamic instabilities are mainly generated because of the joint effect of different-scale GWs. Isolated parts of GWs have much less contribution to the generation of both convective and dynamic instabilities. The dynamic instability is mainly contributed from less stable stratification and large wind shear together. Either factor can lead to about 15% of dynamic instability.

1. Introduction

It is widely known that gravity waves (GWs) transport their energy and momentum from the lower atmosphere to the mesosphere and lower thermosphere (MLT). As these waves reach large amplitudes, they dissipate and deposit energy and momentum in this region, impart significant forcing to the global atmospheric circulation. GWs are dissipated primarily through instability processes: convective instability (CI) that occurs when large-amplitude waves create a negative vertical potential temperature gradient (Hodges, 1967), and dynamic (shear) instability (DI) when a large vertical gradient of horizontal wind is created by wave motion or momentum deposition (Fritts & Rastogi, 1985). Other instability processes could happen under specific conditions, such as vortical-pair instability (Dong & Yeh, 1988), parametric instability (Klostermeyer, 1991), slantwise dynamic instability (Hines, 1971), and resonant instability (Phillips, 1977).

Multiple theories have been proposed to describe the links between waves and instabilities. Lindzen (1981)' linear GW saturation theory provided a simple way to explain the formation of GW breaking, instabilities, and turbulence (Fritts, 1984; Tsuda, 2014). Lindzen (1981) applied the concept of GW breaking due to instabilities to formulate a self-consistent theory that successfully explained the zonal wind reversal and summer-to-winter meridional circulation in the mesosphere. The linear GW saturation theory predicted that high frequency components of GWs mainly contribute to CI (Fritts, 1984; Tsuda, 2014). Multiple nonlinear saturation theories were also proposed (Dunkerton, 1987; Fritts & Alexander, 2003; Hines, 1991; Klostermeyer, 1991) to explain the relationships between instabilities and nonlinear wave-wave and wave-mean flow interactions that are not accounted for in a linear theory. Both types of theories helped to understand the wave breaking processes and instabilities.

Numerical simulations and observational studies have investigated the contributions to the formation of instabilities based on both linear and nonlinear saturation theories. Simulations suggested that inertia GWs might lead to Kelvin-Helmholtz instability (KHI) (Andreassen et al., 1994, 1998; Fritts & Yuan, 1989). Sonmor and Klaassen (1997) used a Floquet analysis of a monochromatic wave propagating in a uniformly stratified background and found that the generation of different types of instabilities are related to the internal GWs with variable frequencies. Small-amplitude GWs in the absence of environmental variations can lead to instabilities (Fruman & Achatz, 2012; Walterscheid et al., 2013). Yue et al. (2010) found that about 60% of the large wind shear formation is driven by long – period waves such as tidal-period perturbations. Fritts et al. (2018) suggested

that mesosphere inversion layer (MILs) can cause large-amplitude GWs to yield instabilities and turbulence. Andrioli et al. (2017) suggested that GWs with period longer than 30 min be responsible for the presence of long-duration dynamically unstable layers (DULs). Some works addressed the contribution to instability formation from nonlinear saturations. Lombard and Riley (1996) found that two-dimensional instabilities are closely related to second-order wave–wave interactions. Sutherland (2001) found that, in the presence of wave–wave interactions of large amplitude waves, the mean flow experiences significant modifications, which can result in critical-level interactions and CI of the wave field. Gardner et al. (2002) suggested that instability can be generated when the combined perturbations associated with tides and GWs induce large vertical gradients in the horizontal wind and temperature profiles. Li, Liu, Swenson, Hecht, and Robinson (2005) found that wave-mean flow interactions contributed significantly to the generation of strong wind shear (>40 m/s/km) and DULs.

Higher-resolution numerical simulations and observations from more advanced instruments both reveal more complex dynamics related to instability. Liu et al. (1999) suggested that the induced mean flow acceleration due to CI may lead to strong shear, which causes DI at lower altitudes. Two-dimensional model result (Liu et al., 2014) showed that the momentum deposited by breaking GWs accelerates the mean wind, creating a background condition that favors the occurrence of instability. She et al. (2004) found that dynamic instability occurs simultaneously with the destruction of the wave train associated with a mesospheric bore. Yuan et al. (2014) found the development and presence of an unstable region around 2 km above the mesospheric inversion layer peak amplitudes. Cai et al. (2014) found when large amplitude GWs are superimposed on tidal wind produced a transient dynamically unstable (DU) region that caused breaking of a subsequent small-scale GW. Hecht et al. (2014) reported a life cycle of instability features measured by Aerospace Corporation's Nightglow Imager. The stability in their study is more dependent on the lapse rate than on the shear. They investigated the formation of KHI, instability features dissipation and secondary instabilities through both observation and direct numerical simulation model. Yuan et al. (2016) reported an event of a dispersing GW spectrum in the mesopause region captured Na lidar at Utah State University. They suggested that GWs being shifted to smaller vertical wavelength may induce some form of instability. The influence of instabilities have been studied as well. Carvalho et al. (2017) supported that ripple structures could be generated in the MLT region due to CI from one-night airglow images observation.

While theoretical and modeling studies have provided much insights into what types of instabilities could happen in different conditions and how they develop, there are rare observational evidences of the frequencies these instabilities actually happen. The occurrence frequencies of these instabilities directly affect the net effect of GW breaking. Due to the highly intermittent nature of GWs (e.g., Cao & Liu, 2016; Conte et al., 2022; Hertzog et al., 2012; Wright et al., 2013), the instabilities are expected to happen intermittently as well. Observationally, while it is now possible to directly observe GW breaking using high resolution imaging (Hecht et al., 2021), it is impossible to detect all GW breaking events even at a single location, due to limitations of instrument operation time and resolutions.

To estimate the occurrence probabilities of instabilities, we can use the atmospheric stability parameters as a proxy, namely the square of buoyancy frequency (N^2) and the Richardson number (Ri). Although stable and unstable conditions described by stability parameters do not always correspond to the absence and presence of instabilities (Achatz, 2007), these are the best ones that can be measured. The observational data needed to calculate N^2 and Ri are high temporal and vertical resolution profiles of temperature and horizontal wind in the MLT, which are not widely available. The only technique that can currently make such measurements is the narrow-band Doppler resonance-fluorescence lidar, which probe the naturally occurring metal layers in the 80–110 km altitude region using lasers that excite specific metal atoms and detect their fluorescence signals (She et al., 2021, and references therein). The lasers must have narrow enough line width (<100 MHz) to be able to probe both Doppler broadening and Doppler shift of the atomic spectral line to infer both temperature and wind simultaneously. The most common metal probed is sodium (Na), due to its large cross section and high abundance in the mesopause region. The lidars also have to achieve high signal-to-noise ratio (SNR) to infer wind and temperature at sufficiently high resolutions to resolve GWs, typically on the order of ∼1 km in vertical and ∼1 min in time.

One of the first stability measurements based on lidar observations was made by a Na lidar at Starfire Optical Range (SOR), new Mexico, which achieved high SNR by using a the 3.5 m astronomical telescope at the site. Zhao et al. (2003) used 32 nights (195 hr) of its observations (at 90-s and 500-m resolutions) to examine atmospheric stabilities at SOR (35°N, 105°W), and found that the atmosphere is most likely to be unstable in winter

Table 1
Total Numbers of Nights of Lidar Measurements From May 2014 to September 2019 at ALO in Each Calendar Month

	January	February	March	April	May	June	July	August	September	October	November	December
Nights	29	20	25	33	16	17	25	22	12	9	24	12
(With *U*, *V*)	(4)	(6)	(14)	(25)	(11)	(17)	(25)	(11)	(5)	(8)	(24)	(10)

Note. These are the nights used to calculate N^2. The numbers in the parentheses are total nights when horizontal wind measurements were available. These are the nights used for wind shear and *Ri* calculations.

and least likely in summer. Li, Liu, and Swenson (2005) analyzed 19 nights (133 hr) of lidar data acquired by the same Na lidar operated at Maui, HI (20°N) with a 3.67-m telescope, at 15-min and 500-m resolutions. They found that most of the convectively unstable (CU) and DU layers are located above the MILs with a tendency for the DU layers to develop below the CU layers. Li, She, et al. (2005) found mesospheric ripples were induced by convective and dynamic instabilities in different nights. They found the probabilities of CI and DI for the respective nights were 12.7% and 14.4% and 5.5% and 17.2%. Using 1 year of data, Sherman and She (2006) presented the vertical variations of the probabilities of large wind shears, DI and CI over Fort Collins, CO (41°N, 105°W) based on Na lidar measurement at resolutions of 15 min and 2 km). They found at a given altitude, the probability of CI is less than 1.4% for all seasons and the probability of DI ranges from 2.7% to 6.0%. More recently, Andrioli et al. (2017) studied the probabilities of the occurrence of CI and DI and their vertical distributions at São José dos Campos (23.1°S, 45.9°W). They used a Na lidar that measured temperature at 300-m and 3-min resolutions, and supplemented with wind measured by a meteor radar located at Cachoeira Paulista (22.7°S, 45°W) at 1-hr and 2-km resolutions. Based on 79 nights (589 hr) of simultaneous data, they found CI presents much more seasonal variability than DI.

The purpose of this study is to present a stability analysis using a set of high quality, extensive lidar data set obtained at the Andes Lidar Observatory in Cerro Pachòn, Chile. The data used was acquired by a high-performance Na lidar on 244 nights over 5 years with a total of 2,170 hr. This high quality data set allows us to not only examine the overall stability properties but also investigate the effects of GWs in different frequency ranges on the generation of unstable regions. The location of the site, in the Andes, is also a special region where many GWs are generated by the high Andes mountains so this analysis provides estimates of instability probabilities due to GWs from a different source than many previous studies.

The paper is organized as following. Section 2 describes the ALO lidar data of temperature and winds and the process applied to calculate the stability parameters. In Section 3, we present the probability distributions of stability parameters. The contributions from GWs to the occurrence of instabilities are given in Section 4. In Section 5, the contributions to DI from stratification and wind shear are described. The results are further discussed in Section 6. Conclusions are presented in Section 7. Finally, in Appendix A, the numerical method for bias correction in calculating probabilities of instabilities is described in detail.

2. Lidar Data and Calculation of Stability Parameters

2.1. Lidar Data

The measurements of temperature and winds used for stability analysis are acquired with the Na lidar at Andes Lidar Observatory located at Cerro Pachón, Chile (30.3°S, 70.7°W). The lidar's large power aperture product (0.66 Wm^{-2}), reliable solid state laser, and efficient receiver optics (Liu et al., 2016), combined with the high elevation site in the Andes with year around clear sky, make it feasible to acquire many nights of measurements at high temporal and spatial resolutions (Guo & Liu, 2021; Guo et al., 2017; Huang et al., 2021). In a normal operation mode, the laser beam was pointed toward zenith (Z), and 20° off zenith toward east (E) and south (S) in zenith-south-zenith-east sequence with typically 60-s interval at each direction. Thus the 3D data has temporal resolution around 4 min. This mode is used to measure temperature and all three wind components. On some nights, the laser beam was pointed to zenith only to make temperature and vertical wind measurements at higher temporal resolution which is about 1 min for acceptable uncertainties. Horizontal winds measurements are not available for those nights. For this study, a total of 2,170 hr of measurements from 244 nights, from May 2014 to September 2019, are used. The total number of nights in each calendar month is summarized in Table 1,

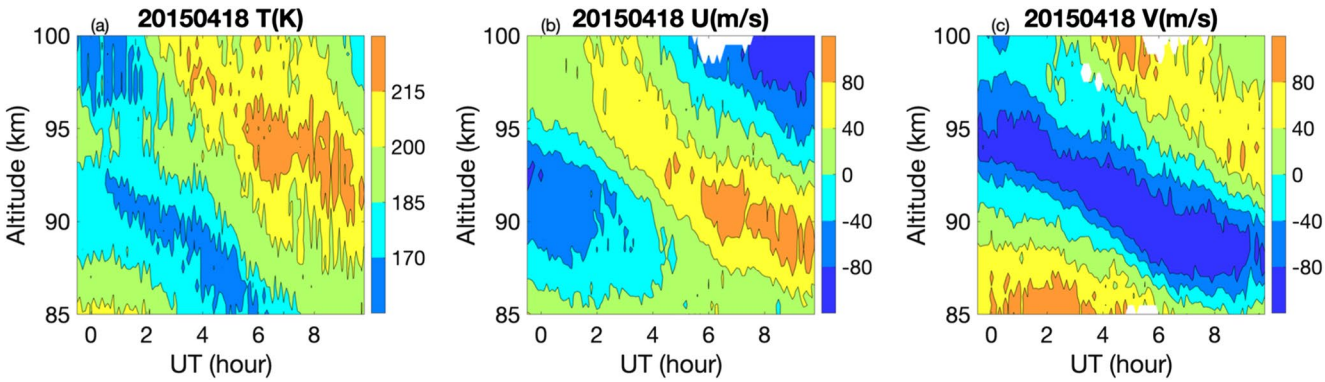

Figure 1. ALO Na Lidar measured *T*, *U* and *V* on 18 April 2015.

together with the numbers of nights when horizontal wind are available. An example of one night measurements of temperature and horizontal wind acquired on 18 April 2015 are shown in Figure 1.

The lidar system obtained raw photon count data at 6-s temporal and 25-m range resolutions, which are then binned to 60-s temporal and 500-m vertical resolutions to derive the temperature and line-of-sight (LOS) winds. At these resolutions, the typical root mean square (rms) errors for temperature and winds in the 85 and 100 km altitude range due to photon noise are no more than 2 K and 6 m s^{-1}, respectively. The error in horizontal wind is the error in LOS wind divided by sin 20°.

Errors grow fast beyond this altitude range because of the decreased Na density. We limit our analysis to the 85–100 km range and exclude measurements with large errors (horizontal wind error >20 m/s; temperature error >10 K. 95% of data are retained with errors less than these 2 values.).

Temperatures and winds are further interpolated to uniform altitude and time intervals at 0.1 hr and 500 m to facilitate calculation of stability parameters. The smallest temporal and vertical scales that can be resolved by the data are 12 min and 1 km, respectively.

2.2. Stability Parameters

The convective stability is measured by the square of buoyancy frequency *N* as

$$N^2 = \frac{g}{T}\left(\frac{\partial T}{\partial z} + \frac{g}{C_p}\right), \tag{1}$$

where $g = 9.5\ \mathrm{ms}^{-2}$ is the gravitational acceleration at the mesopause; *T* is atmospheric temperature; *z* is altitude; $C_p = 1{,}004\ \mathrm{Jkg}^{-1}\ \mathrm{K}^{-1}$ is atmospheric specific heat at constant pressure. When N^2 is negative, the atmosphere is CU and has a super-adiabatic lapse rate ($-\partial T/\partial z > g/C_p$).

The dynamic stability is measured by the Richardson number *Ri* (Miles, 1961) as

$$Ri = \frac{N^2}{S^2}, \tag{2}$$

where

$$S = \left[\left(\frac{dU}{dz}\right)^2 + \left(\frac{dV}{dz}\right)^2\right]^{1/2} \tag{3}$$

is the total vertical shear of horizontal wind and *U* and *V* are zonal and meridional wind speeds, respectively. $Ri < 0$ is equivalent to $N^2 < 0$, indicating CU condition. When $0 < Ri < 0.25$, the atmosphere is considered as DU (Dutton, 1986; Miles & Howard, 1964). Since a small positive *Ri* can be due to a very small positive N^2 and/or large wind shear *S*, to further distinguish these two factors, we will also analyze S, together with N^2 and *Ri*. Since for the nominal value of N^2 is $4 \times 10^{-4}\ \mathrm{s}^{-2}$ (Hirota et al., 1983; Li, Liu, & Swenson, 2005; Taylor &

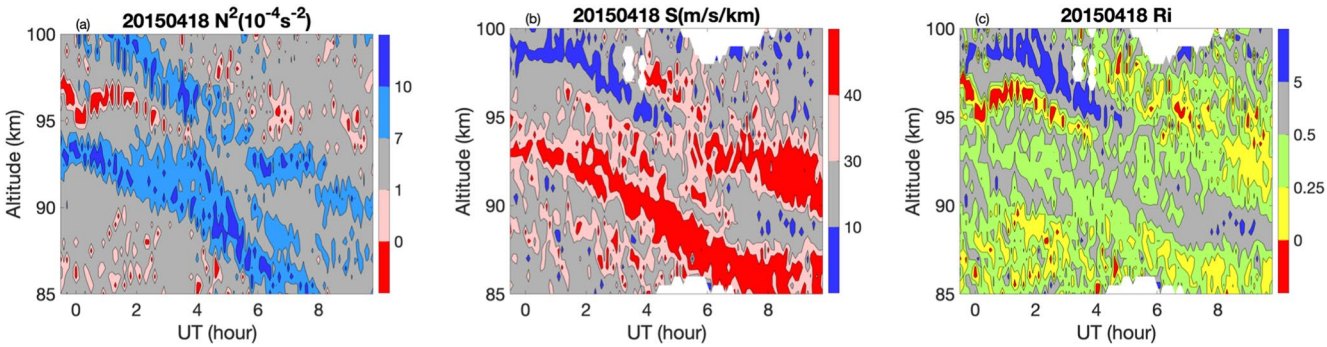

Figure 2. Time-altitude contours of N^2, S and Ri on 18 April 2015 at ALO.

Hapgood, 1990), $Ri < 0.25$ requires $S > 40$ m s^{-1} km^{-1}, we use this value as the threshold to define large and small wind shears.

The numerical calculation of these parameters involves vertical derivatives of T, U and V, which are calculated using centered difference in vertical. For example, N^2 at height level k is calculated as

$$N_k^2 = \frac{g}{T_k}\left(\frac{T_{k+1} - T_{k-1}}{2\Delta z} + \frac{g}{C_p}\right), \tag{4}$$

where $\Delta z = z_k - z_{k-1}$ is the vertical interval. The errors of calculated N^2, S, and Ri come from the errors in measured T, U and V. The effect of these errors on the stability analysis is significant and is discussed in more detail in Appendix A. The most important consequence of the measurement error is that they create a large bias in the calculated probability of instabilities and they have to be corrected. All results presented in this work were corrected for this bias according to the method described in Appendix A.

An example of the three stability parameters derived from the same night of lidar measurements in Figure 1 is shown in Figure 2. In the N^2 plot, large blue areas indicate very stable layers with large N^2 values ($N^2 > 7 \times 10^{-4}$ s^{-2}). The blue regions are moving downward over the night, suggesting the possible influence of tides. Red color indicates CU regions where $N^2 < 0$. In general, the CI does not happen very often, as indicated by the much smaller area of red regions. However, there is one such region between 95 and 97 km that lasts over 2 hr before 2 UT on this night.

The middle contour plot in Figure 2 shows the wind shear S, where red regions represent large wind shear ($S > 40$ ms^{-1} km^{-1}). Just like the blue regions in the N^2 plot, these large wind shear regions are possibly influenced by the tides, and following closely with the region of high N^2. This is expected because only high N^2 region can sustain high S to avoid it being destructed by dynamic instability. The similar features were found in lidar observations at Maui (Li, Liu, & Swenson, 2005) and simulations with the Whole Atmosphere Community Climate Model (Liu, 2017).

The right contour plot shows Ri, in which the red areas are by definition the same as those in the N^2 plot. The yellow areas are DU where Ri is between 0 and 0.25. The yellow areas appeared intermittently, mainly in the regions of large wind shear, and are overall more frequent than regions of negative N^2.

3. Distributions of Stability Parameters

For the purpose of this study, we define high-frequency (HF), medium frequency (MF) and low-frequency (LF) GWs as with the observed periods less than 1 hr, between 1 and 6 hr, and longer than 6 hr, respectively. Our goal here is to isolate the effects on stability properties due to GWs in each frequency range. Although such separation does not take into account of the Doppler effect of the background wind on the intrinsic periods, it is not expected to have much meaningful impact of the overall stability assessment because (a) this Doppler effect changes the intrinsic periods both ways depending on the relative direction of GW propagation and the background, and (b) the effect is not significant for fast GWs. The details of separating waves in these three frequency ranges is described in Section 4.

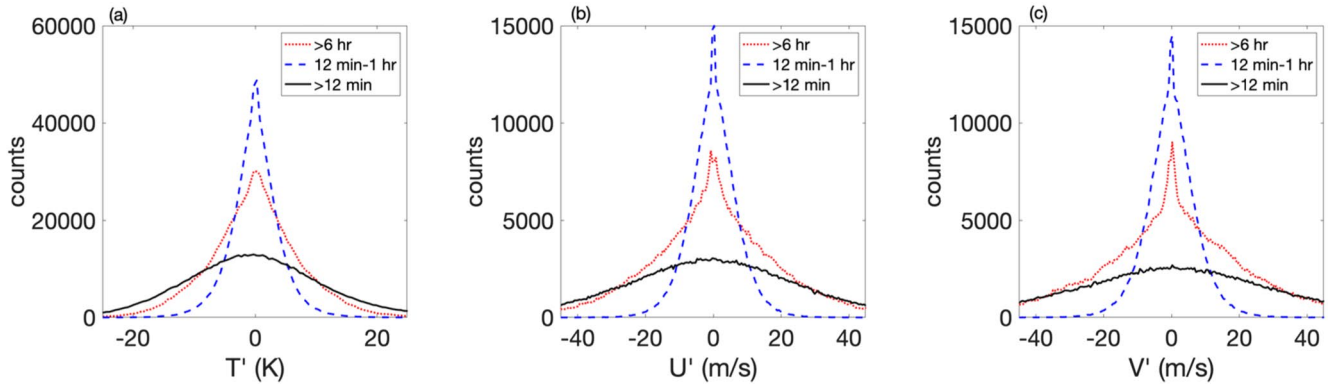

Figure 3. Histograms of T', U' and V' based on counts of gridded data points from all lidar measurements between 85 and 100 km. The bin sizes are 0.5 K, 0.5 ms^{-1} and 0.5 ms^{-1}, respectively. Black solid lines, red dotted lines, and blue dashed lines are distributions of full perturbations, perturbations with period >6 hr (LF GWs); and perturbations with period <1 hr (HF GWs), respectively.

To examine the characteristics of perturbations and the stability parameters, their values at all gridded data points in time-altitude domain (between 85 and 100 km) on all nights are accumulated to construct histograms. The histograms of perturbations of T, U and V, denoted as T', U' and V' respectively, are shown in Figure 3. The three distributions in each plot corresponds to full perturbations, LF perturbations, and HF perturbations (see Figure 3 caption for details). In Figure 3, the x axes represent the perturbations of T, U and V, with bin sizes of 0.5 K, 0.5 ms^{-1} and 0.5 ms^{-1}, respectively. The y axis is the number of data points in the time-altitude domain at 0.1 hr and 500 m resolutions as described at the end of Section 2.1. The values represented by the curves are the numbers of data points within each bin value range. The areas below the curves are the total number of data points, which is the same for all curves in each panel. Because horizontal wind measurements are not available on all nights, the data points for T' are more than those for U' and V'. As expected, the full perturbations have the widest distribution, and both HF and LF histograms are narrower. The LF histograms (red dotted lines) are wider than HF ones (blue dashed lines), indicating that LF perturbations have larger amplitudes than HF ones. Note that the distributions of full perturbations (black solid lines) closely follow a Gaussian distribution, which is in agreement with previous lidar measurements (Gardner & Yang, 1998).

The stability parameters N^2, S and Ri are nonlinear functions of T, U and V so their distributions are non-Gaussian and asymmetric. Their distributions are shown with their histograms in Figure 4. The colors and styles represent the same perturbations as in Figure 3. Here we focus on the distributions when all perturbations are included (black solid lines). Since the variation of N^2 is dominated by $\partial T/\partial z$ in Equation 1, its distribution is nearly Gaussian but with a longer tail on the positive side. It peaks at 3.2×10^{-4} s^{-2} with a median value of 4.2×10^{-4} s^{-2}. The total wind shear S is a positive-definite quantity and its histogram is asymmetric with a longer positive tail. It

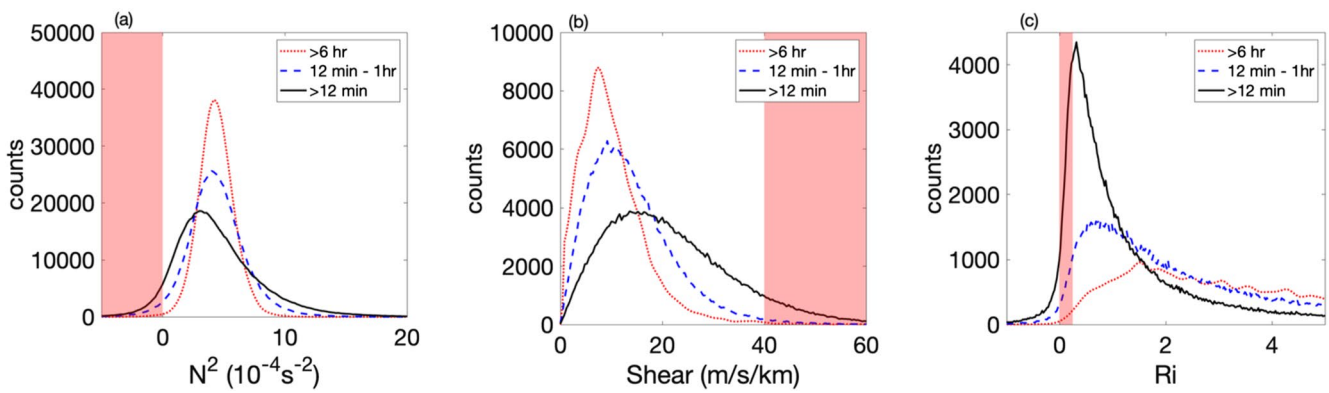

Figure 4. Histograms of (a) N^2, (b) S and (c) Ri. The bin sizes are 0.2×10^{-4} s^{-2}, 0.4 ms^{-1} km^{-1} and 0.02, respectively. Black solid lines are for stability parameters calculated from original lidar measurements which include all waves (with periods >12 min). Red dotted lines are calculated from data with periods >6 hr (LF GWs). Blue dashed lines are calculated from data with periods <1 hr (HF GWs). The shaded regions are $N^2 < 0$, $S > 40$ ms^{-1} km^{-1}, and $0 < Ri < 0.25$, respectively.

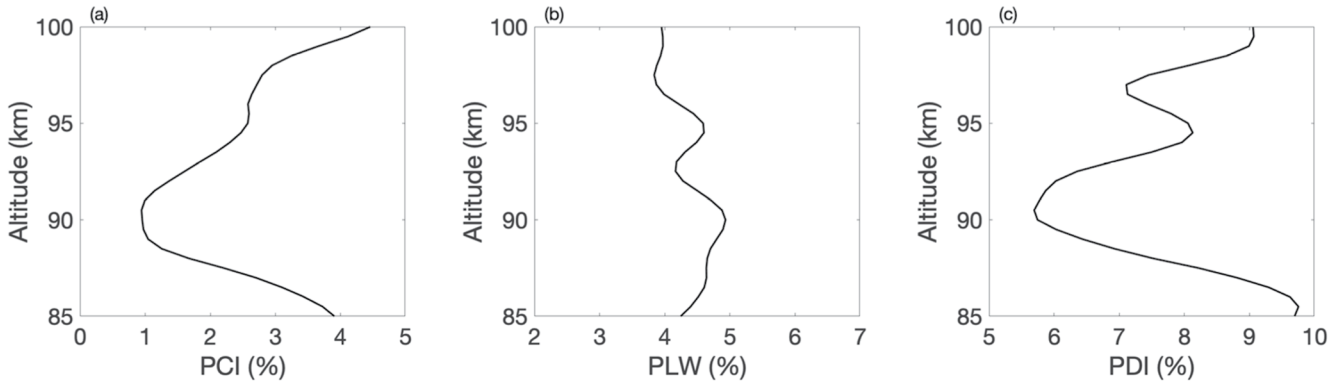

Figure 5. Probability of convective instability (PCI), probability of large wind shear (PLW), and probability of dynamic instability (PDI) as functions of altitudes, calculated from original data (including all waves). The probabilities are calculated using all data within a 3-km altitude bin at each 500 m.

peaks at 16.8 ms^{-1} km^{-1} with a median value of 20.8 ms^{-1} km^{-1}. The *Ri* distribution is highly asymmetric, with a longer tail to the right and a much narrower range to the left. It peaks at 0.32 with a median value of 0.8. In all three histograms, the shaded area indicate negative N^2, $S > 40$ ms^{-1} km^{-1}, and $0 < Ri < 0.25$, corresponding to CU, large wind shear, and DU regions, respectively, and corresponding to the red and yellow regions described earlier for Figure 1.

The likelihood of occurrence of unstable regions or large wind shear is thus defined as the fraction of the area under the distribution curve in the shaded area, which we refer to as the probability of convective instability (PCI), the probability of large wind shear (PLW), and the probability of dynamic instability (PDI), respectively. Note that due to measurement errors, these distributions are wider then their true error-free distributions because of the additional variances from the errors. Therefore, measurement errors introduce a bias in the estimated probabilities. These biases however, can be corrected after careful analysis of the relationship between error magnitudes and biases. This is described in detail in Appendix A. All probability values presented in the paper are bias-corrected. As Figure A1 shows, the biases are very significant especially for PLW and PDI. They all result in an overestimate of the probabilities. Using all lidar measurements, we obtained bias-corrected PCI = 2.7%, PLW = 4.2%, and PDI = 6.7%, with bias correction amounts of 1.7%, 4.5%, 4.4%, respectively. Even with the large bias correction, the DU and large wind shear regions are more likely to occur than CU regions, consistent with the observation in Figure 1.

The vertical distributions of probabilities are shown in Figure 5. The probabilities are calculated with original data (including all waves) for each 3 km vertical bin at every 0.5 km. The PCI has a minimum around 90 km at about 1.6% and increases both above and below this altitude to about 4%–5%. This is consistent with the potential energy density minimum around 90 km measured by USU Na lidar (Cai et al., 2017). The PDI also has a minimum about 5.7% at 90.5 km and increases to about 9.8% at 85.5 km and 9.1% at 100 km. The PLW has little change throughout this altitude region. And Sherman and She (2006) showed similar PCI and PDI profiles shape in Figure 5 in their work, though different magnitude due to the difference in resolution and season. However, above 100 km, we expect PLW to increase due to rapid increase of wind speed above as measured by decades of rockets experiments (Larsen, 2002). The lidar signal limited our analysis to be below 100 km.

4. Gravity Wave Effects on Stability Parameters

4.1. Frequency Dependence of GW Contributions to PCI, PLW and PDI

It is expected that the mean background atmosphere in MLT is stable. Unstable layers occur temporarily and are mostly due to GWs that generate large vertical gradients of temperature and/or horizontal wind. As described in the previous section, we define high-frequency (HF, <1 hr), medium frequency (MF, 1–6 hr) and low-frequency (LF, >6 hr) and assess the effects on stability properties due to GWs in each period range. For reference, the local Coriolis frequency is about 7.29×10^{-5} rad/s and the corresponding period is about 23.9 hr. The specific procedure of separating these GWs are described as following.

Table 2
Changes of Probability of Convective Instability (PCI) When Gravity Waves (GWs) Are Added

PCI(%)	B (0.0%)	BH (1.2%)	BM (0.2%)	BL (0.1%)	BHM (2.1%)	BHL (1.3%)	BML (0.5%)
H	1.2	–	1.9	1.2	–	–	2.2
M	0.2	0.9	–	0.4	–	1.4	–
L	0.1	0.1	0.3	–	0.6	–	–
HM	2.1	–	–	2.6	–	–	–
HL	1.3	–	2.5	–	–	–	–
ML	0.5	1.5	–	–	–	–	–
HML	2.7	–	–	–	–	–	–

Note. The top row indicates the components in the original field with their PCIs indicated in the parentheses. The left column indicates type of GWs added. The values in the table are changes in percentage points of PCI when the GW components indicated by the left column in that row is added to the original field indicated by the top row in that column. For example, the value at the row HM and column B indicates when HF and MF GWs are added to the background, PCI is increased by 2.1 percentage points from 0.0%. See text for detailed description of all notations.

We first filter the original temperature and wind data (denoted as X) with a low-pass 1-hr and a 6-hr full-width Hamming window, and denote the filtered data as X_{1hr} and X_{6hr}, respectively. The nightly averaged wind and temperature are considered to be the background (BG) and denoted as X_B. We can then calculate the follow quantities

$$X_{BH} = X_B + X - X_{1hr},\ X_{BM} = X_B + X_{1hr} - X_{6hr},\ X_{BL} = X_{6hr},$$
$$X_{BHM} = X_B + X - X_{6hr},\ X_{BHL} = X - X_{1hr} + X_{6\,hr},\ X_{BML} = X_{1hr}. \quad (5)$$

where the subscripts denote the components included: B for Background, H for HF GWs, M for MF GWs, and L for LF GWs. For example, X_{BHM} includes the background, HF and MF GWs but not LF GWs. With this notation, the distributions of stability parameters shown in Figure 4 are for X (>12 min), X_{BH} (12 min–1 hr), and X_{BL} (>6 hr).

We calculated the stability parameters for all combination of GWs in Equation 5, and their distributions were obtained. For each distribution, PCI, PLW and PDI were calculated as illustrated in Figure 4. Their differences shown in Figure 4 represent the changes in probabilities when certain types of GWs are added to a field. These probability changes for various scenarios are listed in Tables 2–4. For example, in Table 2, the value in row L and columns BH and BM represent the increase of PCI when LF GWs is added onto BH and BM respectively, leading to their respective PCI increase of 0.1% and of 0.3% respectively (row L; columns BH, BM). There are two clear patterns shown in these tables:

1. For PCI and PDI, HF GWs contribute most to their increase, with MF GWs second, and very little contribution from LF GWs. For PLW, ML GWs contributes most.
2. For all three probabilities, the combined increase of probabilities by two GW components, are always more than the sum of individual contributions from each individual GW component. For example, in Table 4, MF and LF GWs added to the background with HF GWs contribute to 2.0% and 2.4% increase of PDI, respectively (rows H, M; column BL). But when they are both present, the total PDI is increased by 6.2% (row HM; column BL).

The effects of GWs on stabilities can also be understood from the distributions shown in Figure 4, by comparing for example, the black solid line (including all GWs) with the red dotted lines (>6 hr GWs). For N^2, when all waves are included, the distribution is widened and the peak is shifted toward smaller N^2 values, resulting in an increase in PCI. For S, the distribution is also widened and the peak is shifted toward larger S value, resulting in increased PLW. For Ri, the distribution is narrowed (as a result of widened S distribution) with the peak shifted closer to the shaded region where $0 < Ri < 0.25$ and significantly increases PDI.

It is interesting to compare the temperature and wind perturbation distributions in Figure 3 with the N^2 and S distributions in Figures 4a and 4b for LF and HF GWs. While LF perturbations have much larger standard devi-

Table 3
Same as Table 2 but for the Changes of Probability of Large Wind Shear (PLW)

PLW(%)	B (0.3%)	BH (0.3%)	BM (1.1%)	BL (0.9%)	BHM (1.2%)	BHL(1.3%)	BML (3.6%)
H	0.0	–	0.1	0.4	–	–	0.6
M	0.8	0.9	–	2.7	–	2.9	–
L	0.6	1.0	2.5	–	3.0	–	–
HM	0.9	–	–	3.3	–	–	–
HL	1.0	–	3.1	–	–	–	–
ML	3.3	3.9	–	–	–	–	–
HML	3.9	–	–	–	–	–	–

Table 4
Same as Table 2 but for the Changes of Probability of Dynamic Instability (PDI)

PDI(%)	B (0.2%)	BH (1.6%)	BM (0.9%)	BL (0.5%)	BHM (3.4%)	BHL (2.5%)	BML (2.9%)
H	1.4	–	2.5	2.0	–	–	3.8
M	0.7	1.8	–	2.4	–	4.2	–
L	0.3	0.9	2.0	–	3.3	–	–
HM	3.2	–	–	6.2	–	–	–
HL	2.3	–	5.8	–	–	–	–
ML	2.7	5.1	–	–	–	–	–
HML	6.5	–	–	–	–	–	–

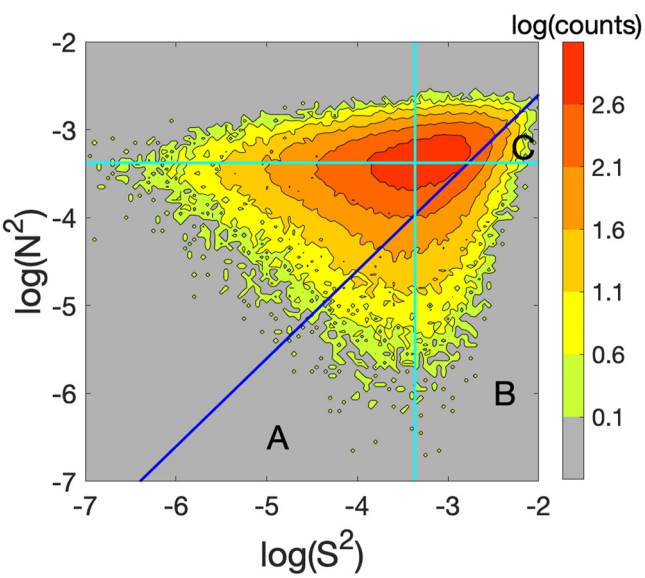

Figure 6. 2D histogram of all data points as a function of both log S^2 and log N^2. The blue diagonal line represents where $Ri = 0.25$. The cyan horizontal and vertical lines indicate medium values of $N^2 = 4.2 \times 10^{-4}$ s^{-2} and $S = 20.8$ ms^{-1} km^{-1}, respectively. The color shades are linear in log(counts) as indicated by the color bar. The bin sizes are both 0.05 for horizontal and vertical axis.

ations or amplitudes, their N^2 and S distributions are much narrower than HF perturbations. This is a clear indication that wave amplitude alone is not a deciding factor for creating unstable layers. The vertical scale of the perturbations is an important factor because it directly affects the lapse rate and vertical wind shear. Our results imply that for waves that can be resolved by the lidar measurements, HF GWs tend to have smaller vertical scales, which result in larger vertical gradients that LF GWs. Even though HF GWs have in general smaller amplitudes compared with LF GWs, the increase in gradients creates both more stable and unstable regions, thus widens the N^2 and S distributions and increases all three probabilities.

4.2. Contributions From N^2 and S to PDI

The measure of PDI is based on $Ri = N^2/S^2$, which is related to both static stability N^2 and vertical shear of horizontal wind S. $0 < Ri < 0.25$ can be satisfied by small positive N^2 and/or large S. In reality, when N^2 positive but close to zero, CI is more likely to occur than dynamic instability because any small perturbations could push N^2 to negative value. Uncertainty in measurements also adds to the uncertainty of whether N^2 is truely positive. Therefore, if a region that satisfies $0 < Ri < 0.25$ is only associated with small positive N^2 but not large S, it should be considered as being near CU, but not DU. A more accurate estimate of the PDI should exclude such regions.

To consider the contributions to a small Ri from N^2 and S separately, we can Equation 2 as

$$\log Ri = \log N^2 - \log S^2, \tag{6}$$

which shows that log Ri is sum of contributions from log N^2 and log S^2. Figure 6 shows 2D histogram of all data points with log N^2 and log S^2 as horizontal and vertical axes, respectively. Data points with $N^2 < 0$ are excluded in this plot. The blue diagonal line corresponds to $Ri = 0.25$. Area below this line is DU ($0 < Ri < 0.25$). The cyan horizontal and vertical lines indicate medium values of $N^2 = 4.2 \times 10^{-4}$ s^{-2} and $S = 20.8$ ms^{-1} km^{-1}, respectively. They separate the area below the diagonal line into three areas, marked as A, B and C. Area A is where N^2 is small and S is small; area B is where N^2 is small and S is large; area C is where N^2 is large and S is large. They make up 17%, 69%, and 14% respectively to the total data points below the diagonal line. This shows that the majority (69%) of data points with $0 < Ri < 0.25$ correspond to large wind shear in a less stable stratification. A small fraction (14%) is due to even larger wind shear in a more stable stratification. A small but not insignificant portion (17%) is due to small N^2 in the absence of large wind shear, which as described above, should not be considered as DU. Therefore, all the PDI values we presented above slightly overestimate the actual probably of dynamic instability due to large wind shear only. The total PDI, if taking this into account, should be 6.7%×(1%–17%) = 5.6%.

5. Discussion

Dynamic instability is much more likely to occur than CI. This is similar to the results at Fort Collins (41°N, 105°W) (Sherman & She, 2006). With 1 year, 390 hr of data, Sherman and She (2006) in their Table 2 reported a mean PCI of 0.88% (0.31%) and PDI of 4.41% (2.73%) with 2 km and 15 min (60 min) resolution, revealing the effect of resolution on the probabilities of instability. Later, Yue et al. (2010), using 1,600 hr of nighttime observations in 3 years with 2 km and 15 min resolution, reported PDI as a function of wind shears in their Table 3, yielding a mean PDI of 9.46%. Judging from the scatter plots in their Figures 6–8, the PCI occurs much less frequently. At Sao Jose dos Campo (23.1°S, 45.5°W) where Andrioli et al. (2017) obtained PCI of 3% and PDI of 17.5%, although these analyses were made with data at

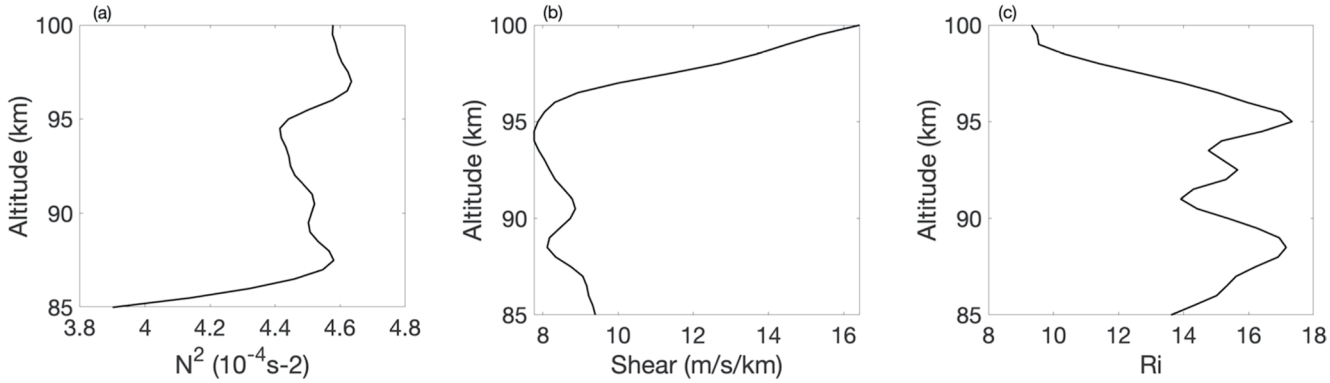

Figure 7. Averaged N^2, S and Ri profiles calculated with nightly averaged T, U, V. The plots show the contributions on N^2, S and Ri from back ground. At 100 km, N^2 is large, which means the back ground is more likely to be convectively stable. At 100 km, the background wind shear is large, which makes it easy to become dynamically unstable.

coarser resolutions (0.5 hr and 2 km). Both PCI and PDI from our measurements are comparable to their results, which suggest the short-period and small-vertical-scale GWs (12–30 min and 0.5 km 2 km) has small or negative contribution on the formation of dynamic instability. More studies are necessary in order to clarify the contributions on the formation of instabilities from different spatial scales and different periods with more complicated classification.

There may be different reasons for large PCI and PDI above/below 90 km. As shown in Figure 7, N^2 is small around 87 km. At 87 km the background temperature is not very convectively stable. Small perturbation can make it convectively and DU. The averaged N^2 are large around 100 km. So the background temperature is stable. But the wave activity is strong at this altitude as shown in Figure 8. So the wave activity is responsible for the large PCI above 90 km. For PDI, the wind shear is larger at 100 km than that at 87 km as well. So the background wind and strong wave activities lead to large PDI together.

The contributions of GWs on probabilities of instabilities were analyzed by separating the data in to HF, MF and LF and background, and separately calculating the probabilities. We found that the HF GWs play the most important role in the increase of PCI and PDI, and LF GWs contribute the least. Our analyses also suggest that two GW components always contribute more on the increase of these probabilities than the sum of increases from each GW component. For example, HF and MF GWs added to the background with LF GWs contribute to 2.0% and 2.4% increase of PDI, respectively. But when they are both present, the total PDI is increased by 6.2%. Yue et al. (2010) reported tides can contribute significantly to the large wind shears in the MLT. Zhao et al. (2003) reported that tides alone are usually not strong enough to induce instability, but they can establish the environment for instabilities to develop. These results are consistent with our findings and support the notion that simultaneous presence of waves at multiple time scales can significantly increase the probabilities of instabilities. In some

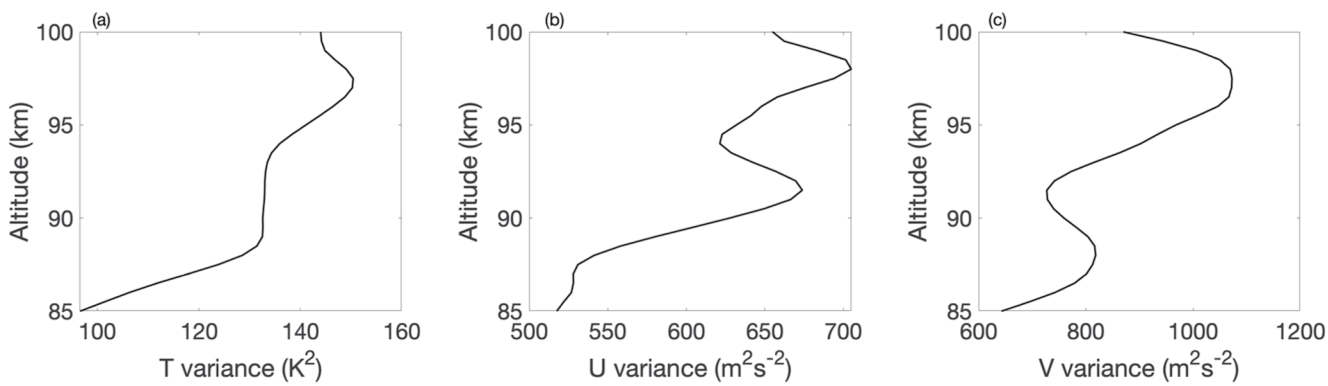

Figure 8. Averaged variances of T, U, V. The plots show the strength of wave activities. The wave activities are stronger at around 100 km than that at other altitude.

cases, wind shear due to one component of GWs are not strong enough for the generation of instabilities. Superposition of waves is more likely to increase the occurrence of locally large wind shear. Heale and Snively (2018) suggested that a LF wave has a significant influence in preventing the HF wave momentum and energy from reaching the upper portions of the thermosphere. HF and MF GWs are more likely to break around mesopause with LF GWs present because the HF and MF waves can be strongly critical-level filtered by the strong winds associated with the LF wave.

HF GWs largely contribute to unstable layers because of their small vertical scale. As shown in Figure 3, distribution of LF T' is broader than that of HF T', which indicate that the magnitude of T' due to HF GWs is smaller than that due to LF GWs. On the other hand, HF GWs contribute more in the formation of negative N^2 than LF GWs, which must be due to larger dT/dz in HF GWs. Therefore, HF GWs must have smaller vertical scales. Although it is generally believed that HF GWs have longer vertical wavelength, this seems not to be the case in this lidar observation. One reason is that LF GWs that have small vertical wave scales are less likely to propagate into the mesopause region because they are strongly dissipated at lower altitudes. The other reason is that vertical extend (15 km) of observation limits the detectable waves to those with vertical wavelength within 15 km.

6. Conclusion

In this paper, we presented analyses of the probabilities of convective and large wind shear and dynamic instabilities (PCI, PLW, PDI) in the mesopause region over the Andes using 2,170 hr of high resolution temperature and wind measurements from a Na lidar at ALO. The data was acquired over 5 years in 244 nights and covers all calendar months. These three probabilities corresponds to $N^2 < 0$, $S > 40$ ms^{-1}, and $0 < Ri < 0.25$, respectively. Biases in these probabilities due to measurement errors were carefully analyzed and found to be significant but could be eliminated. The overall PCI, PLW, and PDI from all lidar data are 2.7%, 4.2%, and 6.7%, respectively, which shows that dynamical instability is more likely to occur than CI.

We separated the data in to HF, MF, and LF and background, and separately calculated the probabilities to examine the impacts of GWs on these probabilities. We found that HF GWs contribute most to the increase of PCI and PDI, and LF GWs contribute the least. Our analyses also show that the total increase of probabilities by two GW components is always more than the sum of increases from each GW component.

We also found that while LF GWs have much larger amplitudes than HF GWs, they contribute less to the perturbations in N^2 and S than HF GWs. This indicates that it is the small vertical scale of HF GWs that largely contribute to the occurrence of unstable layers. Although LF GWs have large amplitude, their larger vertical scale does not create as large vertical gradients in temperature and horizontal wind needed for instability as HF GWs do.

Appendix A: Bias Correction for Probabilities

The stability parameters have non-negligible errors due to temperature and wind measurement errors which are largely due to photon noise. While the temperature and wind errors are zero-mean random quantities, the errors they introduced in stability parameters are not due to the nonlinear relations between the stability parameters and the wind and temperature. Furthermore, these errors increase the variances of the stability parameters from what otherwise would be only due to gravity wave perturbations. The combined effect of measurement errors is therefore a shift and broadening of the stability parameter distributions. Since the probability of instability is measured by the fraction of stability parameter values within a certain range, the change of the stability parameter distribution due to measurement errors introduces a bias in the calculated probability.

The effect of the errors on the stability parameter distribution can be understood from Figure 4, if we consider higher frequency GW perturbations as "errors" added on top of data without such perturbations. Comparing distributions of N^2, S and Ri for LF GWs (red line) and all waves (black lines), they all become broader as higher frequency GWs are included, and the populations in the shaded areas increase. It is clear that his creates a positive bias of the estimated probabilities. The quantitative value of bias depends not only on the magnitude of the measurement errors, but also on the parameter distribution itself. For example, for a very stable atmosphere where almost all N^2 values are positive, PCI is near zero and measurement errors is not likely to create much bias. For

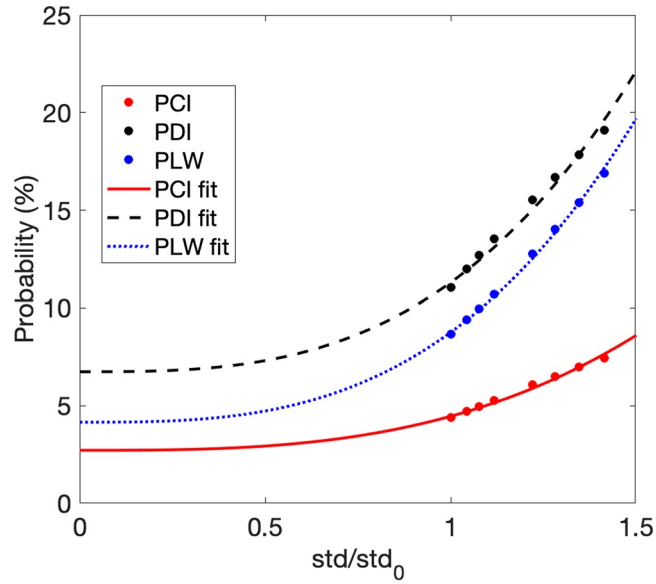

Figure A1. Probability of convective instability (PCI), probability of large wind shear (PLW), and probability of dynamic instability (PDI) with respect to measurement errors with different Gaussian distribution uncertainties. n_σ are factors multiply original uncertainties of T, U and V. Red solid line, black dashed line and blue dotted line are PCI, PDI and PLW with respect to standard deviations, respectively.

PDI, because of the steepness of the Ri distribution in the unstable ($0 < Ri < 0.25$) region, a small broadening may create a large bias.

Bias can be estimated with analytical method with certain assumptions. Analytical bias correction of PCI was presented by Zhao et al. (2003). In their work, the bias of PCI was expressed as a function of the error of N^2, which is assumed to be small, following a Gaussian distribution, and proportional to the temperature error. An analytical formula for the bias of PDI is much harder to obtain and even if possible, would require more assumptions, because Ri is related to both temperature and wind. More assumptions also lead to additional errors in bias estimation.

In this work, we use the Monte-Carlo approach to numerically estimate the bias of PCI, PLW and PDI. This approach is more accurate and does not require many assumptions. The procedure is described as following. For any given set of data, various magnitudes of random errors are added to temperature and wind, and the stability parameters and probabilities of instabilities are re-calculated for each set of random errors added. For each probability calculation, 200 simulation is performed to obtain the mean probability and its standard deviation. The relatively small number of simulation is justifiable because with large number of data points, the probability is a very stable value even when errors at individual data points vary. This is verified by the simulation results that yield a standard deviation of the mean probability always less than 0.01%. As a consequence, we do not show error bars in our probability calculations because they are negligible.

Table A1
Fitted Values of a and b of the Probabilities as Functions of $x = \sigma/\sigma_0$ *as* $ax^3 + b$

Probability (%)	a	b
PCI	1.7 ± 0.1	2.7 ± 0.2
PLW	4.6 ± 0.2	4.2 ± 0.4
PDI	4.6 ± 0.4	6.7 ± 0.7

Note. PCI, probability of convective instability; PDI, probability of dynamic instability; PLW, probability of large wind shear

When adding random errors to the wind and temperature data, one should realize that the effective errors in the data is the combination of the original error already in the data plus and added random error. For example, if the measurement rms error of the original data is σ_0, and random errors with σ_0 rms is added, the resulting error variance of the data becomes $2\sigma_0^2$ and the total rms error becomes $\sigma = \sqrt{2}\sigma_0$. By adding errors at various magnitudes, we obtain the instability probabilities as functions of this total rms error σ. The true bias free probability, is the value when $\sigma = 0$. This probability can be obtained by extrapolating the probabilities from simulations to the point where $\sigma = 0$.

This procedure is illustrated in Figure A1, which is applied to the original data (without any filtering to isolate particular GWs). In the figure, each * represents the probability value at a certain σ, represented as σ/σ_0 (because σ_0 values are different at different data points), where σ_0 is the original measurement rms error. Values at $\sigma/\sigma_0 = 1$ is the original probability without any additional random errors added (thus no simulation needed). Values at $\sigma/\sigma_0 > 1$ are the mean probabilities from simulations with added rms error of $\sigma_0\sqrt{(\sigma/\sigma_0)^2 - 1}$. As expected, the probabilities increase as σ/σ_0 increases. To obtain the probabilities at $\sigma = 0$, we extrapolate the probability values by using a third-order polynomial $ax^3 + b$ (where $x = \sigma/\sigma_0$). With this fitting function, b is the true bias-free probability and $a + b$ is the fitted value of the probability that should be close to that calculated with the original data (without adding any random errors). The fitted parameters are listed in Table A1. Therefore, the true probabilities of PCI, PLW, and PDI are 2.7%, 4.2%, and 6.7%, respectively. The values of a are the biases relative to the fitted values at $\sigma = \sigma_0$. Compared to the original values of 4.4%, 8.7%, 11.1% (which are slightly different from $a + b$), the biases are 1.7%, 4.5%, 4.4%, for PCI, PLW, and PDI, respectively. The much larger bias in PDI is expected based on earlier discussed, due to the steep slope of the *Ri* distribution near the unstable region. Overall, all biases are large, and without correct would lead to a significant overestimate of instability probabilities.

This procedure is repeated for every data set that probably calculated is needed, including GWs in different frequency ranges, as well as data at different altitudes bins. This is necessary because the distributions of the stability parameters are different. Note that when separating data into different frequency ranges, their rms errors are changed due the smoothing process. For example, LF GWs have much smaller error than HF GWs do. Since the filtering process (Hamming window) is precisely known and is a linear function, the rms errors of each data set are readily determined based on the processes they are derived.

Data Availability Statement

The routine ALO Na Lidar data [ALOlidar [2014-present]] between 80 and 105 km and contour plots are available at http://alo.erau.edu/data/nalidar/.

Acknowledgments
This research was supported by National Science Foundation (NSF) grant AGS-1759471. The work by Alan Liu is supported by (while serving at) the NSF. Most of the lidar operations were conducted by Dr. Fabio Vargas and Mr. Carlos Segura. The excellent support to the ALO facility provided by the Association of Universities for Research in Astronomy is acknowledged. Any opinions, findings, and conclusions or recommendations expressed in this material are those of the author(s) and do not necessarily reflect the views of the NSF.

References

Achatz, U. (2007). Gravity-wave breaking: Linear and primary nonlinear dynamics. *Advances in Space Research*, *40*(6), 719–733. https://doi.org/10.1016/j.asr.2007.03.078

ALOlidar (2014-present). Andes lidar observatory.

Andreassen, Ø., Hvidsten, P. Ø., Fritts, D. C., & Arendt, S. (1998). Vorticity dynamics in a breaking internal gravity wave. Part 1. Initial instability evolution. *Journal of Fluid Mechanics*, *367*, 27–46. https://doi.org/10.1017/S0022112098001645

Andreassen, Ø., Wasberg, C. E., Fritts, D. C., & Isler, J. R. (1994). Gravity wave breaking in two and three dimensions: 1. Model description and comparison of two-dimensional evolutions. *Journal of Geophysical Research*, *99*(D4), 8095–8108. https://doi.org/10.1029/93JD03435

Andrioli, V. F., Batista, P. P., Xu, J., Yang, G., Chi, W., & Zhengkuan, L. (2017). Strong temperature gradients and vertical wind shear on MLT region associated to instability source at 23°s. *Journal of Geophysical Research: Space Physics*, *122*(4), 4500–4511. https://doi.org/10.1002/2016JA023638

Cai, X., Yuan, T., & Liu, H.-L. (2017). Large-scale gravity wave perturbations in the mesopause region above northern Hemisphere midlatitudes during autumnal equinox: A joint study by the USU Na lidar and whole atmosphere community climate model. *Annales Geophysicae*, *35*(2), 181–188. https://doi.org/10.5194/angeo-35-181-2017

Cai, X., Yuan, T., Zhao, Y., Pautet, P.-D., Taylor, M. J., & Pendleton, W. R., Jr. (2014). A coordinated investigation of the gravity wave breaking and the associated dynamical instability by a Na lidar and an Advanced Mesosphere Temperature Mapper over Logan, UT (41.7°n, 111.8°w). *Journal of Geophysical Research: Space Physics*, *119*(8), 6852–6864. https://doi.org/10.1002/2014JA020131

Cao, B., & Liu, A. Z. (2016). Intermittency of gravity wave momentum flux in the mesopause region observed with an all-sky airglow imager. *Journal of Geophysical Research: Atmospheres*, *121*(2), 650–663. https://doi.org/10.1002/2015JD023802

Carvalho, A., Paulino, I., Medeiros, A., Lima, L., Buriti, R., Paulino, A., et al. (2017). Case study of convective instability observed in airglow images over the Northeast of Brazil. *Journal of Atmospheric and Solar-Terrestrial Physics*, *154*, 33–42. https://doi.org/10.1016/j.jastp.2016.12.003

Conte, J. F., Chau, J. L., Liu, A., Qiao, Z., Fritts, D. C., Hormaechea, J. L., et al. (2022). Comparison of MLT momentum fluxes over the Andes at four different latitudinal sectors using multistatic radar configurations. *Journal of Geophysical Research: Atmospheres*, *127*(4), e2021JD035. https://doi.org/10.1029/2021jd035982

Dong, B., & Yeh, K. C. (1988). Resonant and nonresonant wave-wave interactions in an isothermal atmosphere. *Journal of Geophysical Research*, *93*(D4), 3729–3744. https://doi.org/10.1029/JD093iD04p03729

Dunkerton, T. J. (1987). Effect of nonlinear instability on gravity-wave momentum transport. *Journal of the Atmospheric Sciences*, *44*(21), 3188–3209. https://doi.org/10.1175/1520-0469(1987)044¡3188:EONIOG¿2.0.CO;2

Dutton, J. (1986). *Dynamics of atmospheric motion* (p. 617). Dover Pubns.

Fritts, D. C. (1984). Gravity wave saturation in the middle atmosphere: A review of theory and observations. *Reviews of Geophysics*, *22*(3), 275–308. https://doi.org/10.1029/RG022i003p00275

Fritts, D. C., & Alexander, M. J. (2003). Gravity wave dynamics and effects in the middle atmosphere. *Reviews of Geophysics*, *41*(1), 1003. https://doi.org/10.1029/2001RG000106

Fritts, D. C., Laughman, B., Wang, L., Lund, T. S., & Collins, R. L. (2018). Gravity wave dynamics in a mesospheric inversion layer: 1. Reflection, trapping, and instability dynamics. *Journal of Geophysical Research: Atmospheres*, *123*(2), 626–648. https://doi.org/10.1002/2017JD027440

Fritts, D. C., & Rastogi, P. K. (1985). Convective and dynamical instabilities due to gravity wave motions in the lower and middle atmosphere: Theory and observations. *Radio Science*, *20*(6), 1247–1277. https://doi.org/10.1029/RS020i006p01247

Fritts, D. C., & Yuan, L. (1989). Stability analysis of inertia-gravity wave structure in the middle atmosphere. *Journal of the Atmospheric Sciences*, *46*(12), 1738–1745. https://doi.org/10.1175/1520-0469(1989)046¡1738:SAOIWS¿2.0.CO;2

Fruman, M. D., & Achatz, U. (2012). Secondary instabilities in breaking inertia–gravity waves. *Journal of the Atmospheric Sciences*, *69*(1), 303–322. https://doi.org/10.1175/JAS-D-10-05027.1

Gardner, C. S., & Yang, W. (1998). Measurements of the dynamical cooling rate associated with the vertical transport of heat by dissipating gravity waves in the mesopause region at the Starfire Optical Range, New Mexico. *Journal of Geophysical Research*, *103*(D14), 16909–16926. https://doi.org/10.1029/98JD00683

Gardner, C. S., Zhao, Y., & Liu, A. Z. (2002). Atmospheric stability and gravity wave dissipation in the mesopause region. *Journal of Atmospheric and Solar-Terrestrial Physics*, *64*(8), 923–929. https://doi.org/10.1016/S1364-6826(02)00047-0

Guo, Y., & Liu, A. Z. (2021). Seasonal variation of vertical heat and energy fluxes due to dissipating gravity waves in the mesopause region over the Andes. *Journal of Geophysical Research: Atmospheres*, *126*(3), e2020JD033825. https://doi.org/10.1029/2020JD033825

Guo, Y., Liu, A. Z., & Gardner, C. S. (2017). First Na lidar measurements of turbulence heat flux, thermal diffusivity, and energy dissipation rate in the mesopause region. *Geophysical Research Letters*, *44*(11), 5782–5790. https://doi.org/10.1002/2017GL073807

Heale, C. J., & Snively, J. B. (2018). A comparison of small- and medium-scale gravity wave interactions in the linear and nonlinear limits. *Journal of Geophysical Research: Atmospheres*, *123*(5), 2454–2474. https://doi.org/10.1002/2017JD027590

Hecht, J. H., Fritts, D. C., Gelinas, L. J., Rudy, R. J., Walterscheid, R. L., & Liu, A. Z. (2021). Kelvin-Helmholtz billow interactions and instabilities in the mesosphere over the Andes Lidar Observatory: 1. Observations. *Journal of Geophysical Research: Atmospheres*, *126*(1), e2020JD033414. https://doi.org/10.1029/2020JD033414

Hecht, J. H., Wan, K., Gelinas, L. J., Fritts, D. C., Walterscheid, R. L., Rudy, R. J., et al. (2014). The life cycle of instability features measured from the Andes Lidar Observatory over Cerro Pachon on 24 March 2012. *Journal of Geophysical Research: Atmospheres*, *119*(14), 8872–8898. https://doi.org/10.1002/2014JD021726

Hertzog, A., Alexander, M. J., & Plougonven, R. (2012). On the intermittency of gravity wave momentum flux in the stratosphere. *Journal of the Atmospheric Sciences*, *69*(11), 3433–3448. https://doi.org/10.1175/jas-d-12-09.1

Hines, C. O. (1971). Generalizations of the Richardson criterion for the onset of atmospheric turbulence. *Quarterly Journal of the Royal Meteorological Society*, *97*(414), 429–439. https://doi.org/10.1002/qj.49709741405

Hines, C. O. (1991). The saturation of gravity waves in the middle atmosphere. Part i: Critique of linear-instability theory. *Journal of the Atmospheric Sciences*, *48*(11), 1348–1359. https://doi.org/10.1175/1520-0469(1991)048¡1348:TSOGWI¿2.0.CO;2

Hirota, I., Maekawa, Y., Fukao, S., Fukuyama, K., Sulzer, M. P., Fellous, J. L., et al. (1983). Fifteen-day observation of mesospheric and lower thermospheric motions with the aid of the Arecibo UHF radar. *Journal of Geophysical Research*, *88*(C11), 6835–6842. https://doi.org/10.1029/JC088iC11p06835

Hodges, R. R., Jr. (1967). Generation of turbulence in the upper atmosphere by internal gravity waves. *Journal of Geophysical Research*, *72*(13), 3455–3458. https://doi.org/10.1029/JZ072i013p03455

Huang, K. M., Liu, H., Liu, A. Z., Zhang, S. D., Huang, C. M., Gong, Y., & Ning, W. H. (2021). Investigation on spectral characteristics of gravity waves in the MLT using lidar observations at Andes. *Journal of Geophysical Research: Space Physics*, *126*(4), e2020JA028918. https://doi.org/10.1029/2020JA028918

Klostermeyer, J. (1991). Two- and three-dimensional parametric instabilities in finite-amplitude internal gravity waves. *Geophysical & Astrophysical Fluid Dynamics*, *61*(1–4), 1–25. https://doi.org/10.1080/03091929108229035

Larsen, M. F. (2002). Winds and shears in the mesosphere and lower thermosphere: Results from four decades of chemical release wind measurements. *Journal of Geophysical Research*, *107*(A8), SIA28-1–SIA28-14. https://doi.org/10.1029/2001JA000218

Li, F., Liu, A. Z., & Swenson, G. R. (2005). Characteristics of instabilities in the mesopause region over Maui, Hawaii. *Journal of Geophysical Research*, *110*(D9), D09S12. https://doi.org/10.1029/2004JD005097

Li, F., Liu, A. Z., Swenson, G. R., Hecht, J. H., & Robinson, W. A. (2005). Observations of gravity wave breakdown into ripples associated with dynamical instabilities. *Journal of Geophysical Research*, *110*(D9), D09S11. https://doi.org/10.1029/2004JD004849

Li, T., She, C. Y., Williams, B. P., Yuan, T., Collins, R. L., Kieffaber, L. M., & Peterson, A. W. (2005). Concurrent OH imager and sodium temperature/wind lidar observation of localized ripples over northern Colorado. *Journal of Geophysical Research*, *110*(D13), D13110. https://doi.org/10.1029/2004JD004885

Lindzen, R. S. (1981). Turbulence and stress owing to gravity wave and tidal breakdown. *Journal of Geophysical Research*, *86*(C10), 9707–9714. https://doi.org/10.1029/JC086iC10p09707

Liu, A. Z., Guo, Y., Vargas, F., & Swenson, G. R. (2016). First measurement of horizontal wind and temperature in the lower thermosphere (105–140 km) with a Na Lidar at Andes Lidar Observatory. *Geophysical Research Letters*, *43*(6), 2374–2380. https://doi.org/10.1002/2016GL068461

Liu, H.-L. (2017). Large wind shears and their implications for diffusion in regions with enhanced static stability: The mesopause and the tropopause. *Journal of Geophysical Research: Atmospheres*, *122*(18), 9579–9590. https://doi.org/10.1002/2017JD026748

Liu, H.-L., Hays, P. B., & Roble, R. G. (1999). A numerical study of gravity wave breaking and impacts on turbulence and mean state. *Journal of the Atmospheric Sciences*, *56*(13), 2152–2177. https://doi.org/10.1175/1520-0469(1999)056¡2152:ANSOGW¿2.0.CO;2

Liu, X., Xu, J., Liu, H.-L., Yue, J., & Yuan, W. (2014). Simulations of large winds and wind shears induced by gravity wave breaking in the mesosphere and lower thermosphere (MLT) region. *Annales Geophysicae*, *32*(5), 543–552. https://doi.org/10.5194/angeo-32-543-2014

Lombard, P. N., & Riley, J. J. (1996). Instability and breakdown of internal gravity waves. I. linear stability analysis. *Physics of Fluids*, *8*(12), 3271–3287. https://doi.org/10.1063/1.869117

Miles, J. W. (1961). On the stability of heterogeneous shear flows. *Journal of Fluid Mechanics*, *10*(4), 496–508. https://doi.org/10.1017/S0022112061000305

Miles, J. W., & Howard, L. N. (1964). Note on a heterogeneous shear flow. *Journal of Fluid Mechanics*, *20*(2), 331–336. https://doi.org/10.1017/S0022112064001252

Phillips, O. M. (1977). *The dynamics of the upper ocean* (2d ed.), (p. 336). Cambridge University Press.

She, C. Y., Li, T., Williams, B. P., Yuan, T., & Picard, R. H. (2004). Concurrent OH imager and sodium temperature/wind lidar observation of a mesopause region undular bore event over fort Collins/Platteville, Colorado. *Journal of Geophysical Research*, *109*(D22), D22107. https://doi.org/10.1029/2004JD004742

She, C.-Y., Liu, A. Z., Yuan, T., Yue, J., Li, T., Ban, C., & Friedman, J. (2021). MLT Science Enabled by Atmospheric Lidars. In W. Wang, Y. Zhang, & L. Paxton (Eds.), *Upper atmosphere dynamics and energetics* (pp. 395–450).

Sherman, J. P., & She, C.-Y. (2006). Seasonal variation of mesopause region wind shears, convective and dynamic instabilities above Fort Collins, CO: A statistical study. *Journal of Atmospheric and Solar-Terrestrial Physics*, *68*(10), 1061–1074. https://doi.org/10.1016/j.jastp.2006.01.011

Sonmor, L. J., & Klaassen, G. P. (1997). Toward a unified theory of gravity wave stability. *Journal of the Atmospheric Sciences*, *54*(22), 2655–2680. https://doi.org/10.1175/1520-0469(1997)054¡2655:TAUTOG¿2.0.CO;2

Sutherland, B. R. (2001). Finite-amplitude internal wavepacket dispersion and breaking. *Journal of Fluid Mechanics*, *429*, 343–380. https://doi.org/10.1017/S0022112000002846

Taylor, M., & Hapgood, M. (1990). On the origin of ripple-type wave structure in the OH nightglow emission. *Planetary and Space Science*, *38*(11), 1421–1430. https://doi.org/10.1016/0032-0633(90)90117-9

Tsuda, T. (2014). Characteristics of atmospheric gravity waves observed using the mu (middle and upper atmosphere) radar and GPS (global positioning system) radio occultation. *Proceedings of the Japan Academy Series B Physical and Biological Sciences*, *90*(1), 12–27. https://doi.org/10.2183/pjab.90.12

Walterscheid, R. L., Gelinas, L. J., Hecht, J. H., & Liu, A. Z. (2013). Instability structures during periods of large richardson number (ri > 1/4): Evidence of parametric instability. *Journal of Geophysical Research: Atmospheres*, *118*(13), 6929–6939. https://doi.org/10.1002/jgrd.50514

Wright, C. J., Osprey, S. M., & Gille, J. C. (2013). Global observations of gravity wave intermittency and its impact on the observed momentum flux morphology. *Journal of Geophysical Research: Atmospheres*, *118*(19), 10980–10993. https://doi.org/10.1002/jgrd.50869

Yuan, T., Heale, C. J., Snively, J. B., Cai, X., Pautet, P.-D., Fish, C., et al. (2016). Evidence of dispersion and refraction of a spectrally broad gravity wave packet in the mesopause region observed by the Na lidar and mesospheric temperature mapper above Logan, Utah. *Journal of Geophysical Research: Atmospheres*, *121*(2), 579–594. https://doi.org/10.1002/2015JD023685

Yuan, T., Pautet, P. D., Zhao, Y., Cai, X., Criddle, N. R., Taylor, M. J., & Pendleton, W. R., Jr. (2014). Coordinated investigation of mid-latitude upper mesospheric temperature inversion layers and the associated gravity wave forcing by Na lidar and Advanced Mesospheric Temperature Mapper in Logan, Utah. *Journal of Geophysical Research: Atmospheres*, *119*(7), 3756–3769. https://doi.org/10.1002/2013JD020586

Yue, J., She, C.-Y., & Liu, H.-L. (2010). Large wind shears and stabilities in the mesopause region observed by Na wind-temperature lidar at midlatitude. *Journal of Geophysical Research*, *115*(A10), A10307. https://doi.org/10.1029/2009JA014864

Zhao, Y., Liu, A. Z., & Gardner, C. S. (2003). Measurements of atmospheric stability in the mesopause region at starfire optical range, NM. *Journal of Atmospheric and Solar-Terrestrial Physics*, *65*(2), 219–232. https://doi.org/10.1016/S1364-6826(02)00288-2